

Tunable Graphene–Silicon Heterojunctions for Ultrasensitive Photodetection

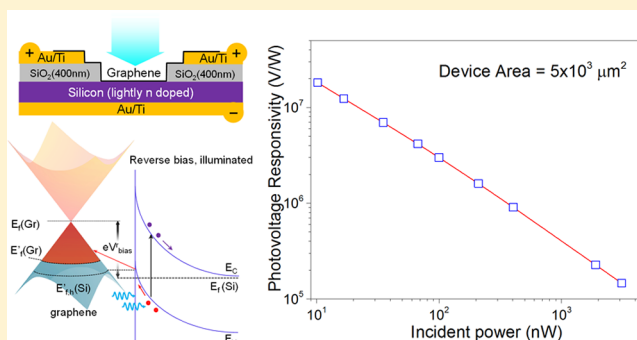
Xiaohong An,^{*,†} Fangze Liu,[†] Yung Joon Jung,[‡] and Swastik Kar^{*,†}

[†]Department of Physics and [‡]Mechanical and Industrial Engineering, Northeastern University, Boston, Massachusetts 02115, United States

S Supporting Information

ABSTRACT: We present the photodetection properties of graphene/Si heterojunctions both in the photocurrent and photovoltage modes. Monolayer graphene/Si junctions were found to be excellent weak-signal detectors with photovoltage responsivity exceeding 10^7 V/W and with noise-equivalent-power reaching ~ 1 pW/Hz^{1/2}, potentially capable of distinguishing materials with transmittance, $T = 0.9995$ in a 0.5 s integration time. In the photocurrent mode, the response was found to remain linear over at least six decades of incident power (P), with tunable responsivity up to 435 mA/W (corresponding to incident photon conversion efficiency (IPCE) $> 65\%$) obtained by layer thickening and doping. With millisecond-scale responses and ON/OFF ratios exceeding 10^4 , these photodiodes are highly suitable for tunable and scalable broadband ($400 < \lambda < 900$ nm) photodetectors, photometers, and millisecond-response switching, spectroscopic and imaging devices, and further, and are architecturally compatible with on-chip low-power optoelectronics.

KEYWORDS: Graphene, photodetection, responsivity, noise equivalent power, specific detectivity



Nanoscale materials, due to their diverse electronic and optical properties, and with a range of architectures, are constantly being explored for an array of low-cost, sensitive, and scalable photodetection technologies.^{1–4} For example, nanowires of conventional semiconductor materials such as Si, Ge, GaN, GaAs, InP, and so forth provide a versatile platform for photodetection, affording direct structural and functional compatibility with existing photonic and optoelectronic circuitry.¹ In contrast, low-cost solution-processable quantum dots are highly appealing due to their potentials for large-area and flexible-electronic applications. Their photoconductive response characterizes high quantum gains resulting in ultrahigh responses ($\sim 10^3$ A/W) and specific detectivities ($\sim 10^{13}$ Jones).² Nanoscale junctions of quantum dots with metals have also been reported to have ultrafast responses of the order of GHz.³ Similarly, carbon nanotubes,⁴ with their extremely narrow diameters and chirality-dependent band-gaps, can be potentially utilized for spectrally selective photodetectors of ultrasmall dimensions.

In this context, graphene-based photon-sensing and photo-switching devices have recently attracted enormous attention for their ultrafast and broadband response.^{5–15} Although these devices are highly appealing for ultrafast optical communications, they suffer limitations for weak signal detection, imaging, and spectroscopic applications due to their low responsivity values. Within the visible to telecommunications-friendly wavelength range (i.e., $400 \text{ nm} \leq \lambda \leq 1550 \text{ nm}$), using both

photovoltaic^{5,10} and photothermoelectric or hot-carrier effects^{9,11,14} along with enhancement techniques including asymmetric metal-contacts,⁶ plasmonic architectures,^{7,8} and microcavity confinements,^{12,13} the photocurrent responsivity ($R_I = I_{ph}/P$) has at best remained limited within $1\text{--}2 \times 10^{-2}$ A/W.^{7,13} These low responses have been primarily attributed to the intrinsically low optical absorption ($\approx 2.3\%$) of graphene¹⁶ along with the absence of any gain mechanisms.

By using graphene as the carrier collector and multiplier, an effective gain mechanism (with $R_I > 10^7$ A/W) was recently reported in graphene/quantum-dot hybrid devices.¹⁵ Despite their appeal for ultraweak signal detection, the responsivity of these devices above $P \approx 10^{-13}$ W fall as $R_I \sim 1/P$, implying a rapid photocurrent saturation above these incident light powers. With considerably large dark currents that render them ineffective as photoswitches (ON/OFF ratio $\ll 1$) and large dark-power consumption, they are impractical for many large-scale applications (such as pixels in imaging devices that require large arrays of photodetectors).

For many applications, photovoltage (instead of photocurrent) measurements are preferred as a sensitive method for photodetection without any Joule-heating associated power consumption. Past works reveal that metal–graphene interfaces

Received: October 3, 2012

Revised: January 22, 2013

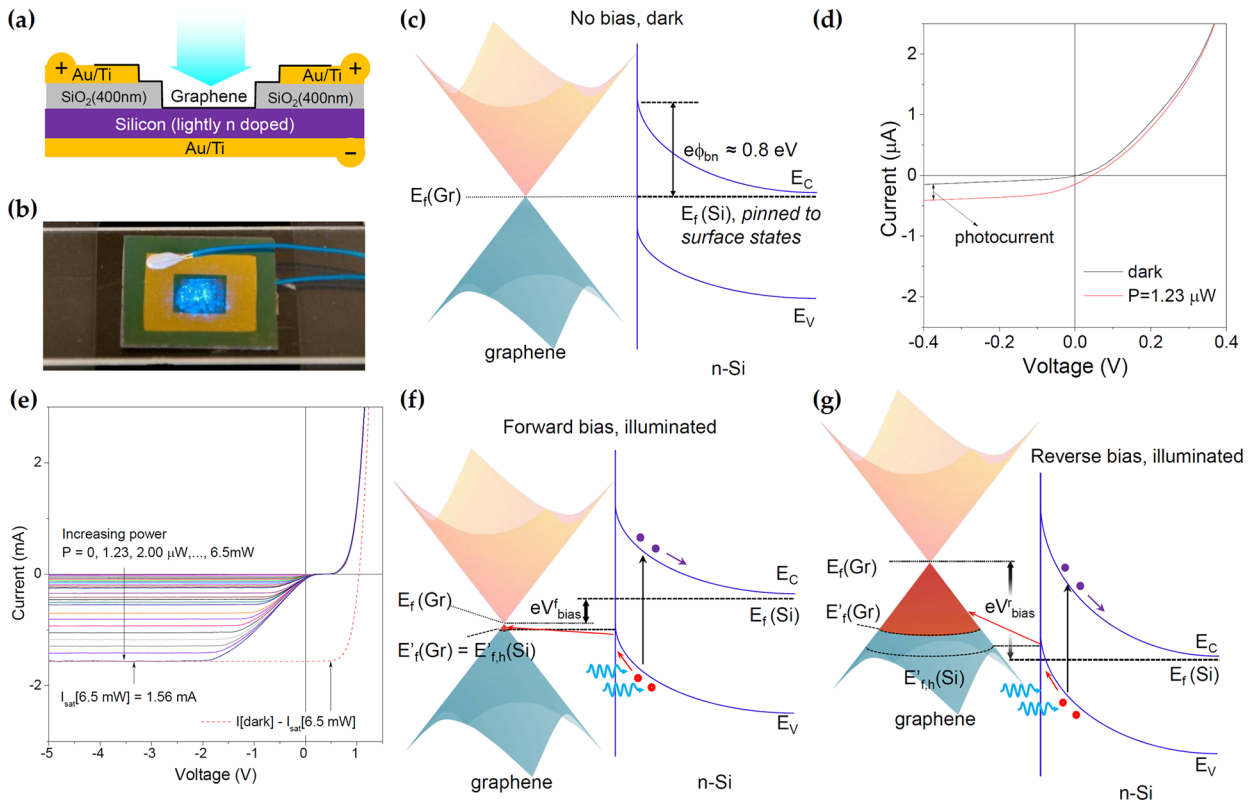


Figure 1. (a) Schematic and (b) a digital photograph of a monolayer graphene (1LG)/Si heterojunction device, with the polarity in part (a) shown for forward bias. (c) Thermal equilibrium energy band diagram of the heterojunction in darkness, with the band profile of n-Si pinned to the charge neutrality level of its own surface states (see text). The dark Fermi level of graphene $E_f(\text{Gr})$ is also shown. (d) Current–voltage (I – V) curves of device A (area = 25 mm^2) under darkness and weak illumination ($P = 1.23 \mu\text{W}$, $\lambda = 488 \text{ nm}$) showing a conventional photodiode-like behavior. (e) Deviation of the I – V curves from a conventional photodiode response as the incident light power is increased up to $P = 6.5 \text{ mW}$. The expected ideal photodiode behavior at $P = 6.5 \text{ mW}$ is plotted with a red dashed line. (f) Schematic showing the application of a forward bias (V_{bias}^f) that lowers $E_f(\text{Gr})$ and reduces the number of accessible states for the injection of photoexcited holes from Si, resulting in the strongly suppressed photocurrent in forward bias seen in part e. The red surface on the Dirac cone of graphene denotes the holes injected from Si and is a measure of the maximum photocurrent when the quasi Fermi level of graphene, $E'_f(\text{Gr})$, aligns with the quasi Fermi level for holes in Si, $E'_{fh}(\text{Si})$. (g) Application of a reverse bias (V_{bias}^r) raises $E_f(\text{Gr})$ and opens up a large number of accessible states that can be occupied by photoexcited holes injected from Si under illumination. This results in the unsuppressed large photocurrents under reverse bias as seen in part e. The external bias controls the position of the Fermi level and hence the number of photoexcited carriers that can inject from Si (i.e., the photocurrent).

can generate photovoltages of $\sim 1 \text{ V/W}$,⁵ which can be enhanced to $\sim 5 \text{ V/W}$ using plasmonic focusing and appropriate gate voltages.⁷ It appears that the limits of photovoltage response for low dark-current graphene-based devices, especially under extremely weak signals (where the high responsivities are more meaningful), have not been critically investigated. Further, most of the above-mentioned devices used mechanically exfoliated graphene,¹⁷ which possess high carrier mobility, but are unsuitable for large-scale deployment. For realistic applications, high-performance devices using large-area chemical vapor deposition (CVD)-grown graphene¹⁸ without complex enhancement architectures^{6–8,12,13} are highly desirable. However, so far, a simple approach for obtaining tunable high-responsivity graphene-based devices with low dark currents, low-power detection limits, and high operational dynamic ranges, using simple, scalable, and potentially low-cost techniques remains undemonstrated.

We show that planar 2D heterojunctions of CVD-grown graphene and Si in a conventional Schottky-diode-like configuration can effectively address these issues, providing a platform for a variety of optoelectronic devices. In these junctions, the photoexcitation resides in Si, while graphene is

the carrier collector. In recent times, a number of works have explored the unique properties of graphene/Si heterojunctions to develop diodes,¹⁹ solar cells,^{20,21} and the so-called “barristor”²²—a variable-barrier switch. However, so far, these junctions have not been examined for ultrasensitive photo-detection for applications such as weak-signal imaging or spectroscopy. Further, in these junctions, low reverse-biases can very effectively manipulate the Fermi-levels of graphene (unlike larger voltages that are required in capacitively coupled gates). The ability to tune the dark Fermi level ($E_f(\text{Gr})$) of graphene and, more importantly, its relative position with respect to the quasi-Fermi level for holes in silicon ($E'_{fh}(\text{Si})$), the modified Fermi level due to the generation of photoexcited holes in Si) is a key mechanism that enables a high degree of tunability and efficient capture of photoexcited carriers, resulting in high photocurrent responsivity values whose performances can be dramatically improved by layer-thickening and simple doping approaches. The tunable photocurrent responsivity is an attractive feature for adjustment to variable-brightness imaging applications. At the same time, these junctions also possess exceptionally high photovoltage response, which increases with decreasing incident power, making it highly suitable as weak-signal detectors in the photovoltage mode. In this work, we

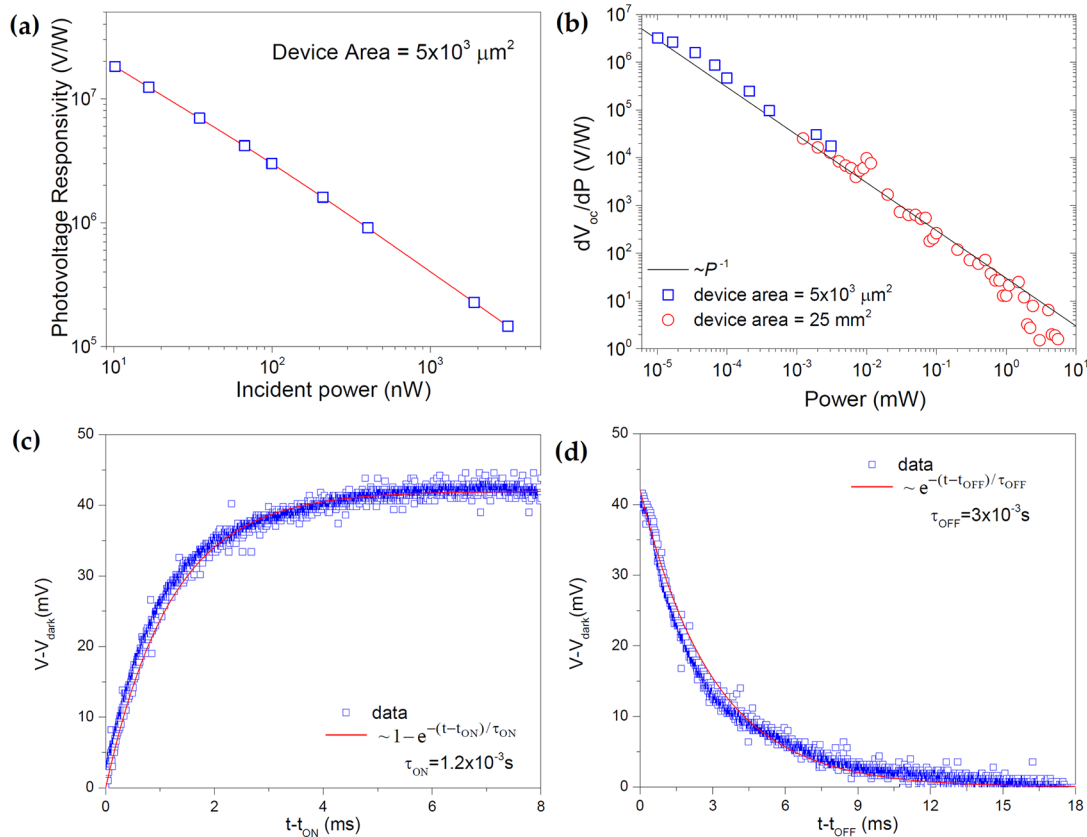


Figure 2. (a) Variation of the voltage responsivity obtained from the open-circuit voltage, V_{OC} , and as a function of incident power, P , in device B. At the lowest powers, the voltage responsivity exceeds 10^7 V/W. (b) Variation of the dynamic photovoltage responsivity (or, the contrast sensitivity dV_{OC}/dP) as a function of P in both devices A and B. In device B, the contrast sensitivity exceeds 10^6 V/W at $P \approx 10$ nW, and the $\sim P^{-1}$ dependence is identical in both devices. The voltage response to (c) turning ON and (d) turning OFF of incident light in device B, showing exponential rise and fall behaviors with millisecond time scales. In all cases, the incident light wavelength was 488 nm.

critically investigate the various important parameters of such applications, such as responsivity, detection limit, switching speed, ON/OFF ratio, spectral bandwidth, contrast sensitivity, and dynamic range in monolayer and few-layered graphene/Si heterojunctions, operating both in photocurrent and photovoltage modes.

The photoresponse behaviors were first tested in monolayer graphene (1LG)/Si devices, and their intrinsic parameters were found to be largely independent of size. We present results from the largest (device A) and the smallest (device B) devices with junction areas = 25 mm^2 and 5000 μm^2 , respectively. We used lightly n-doped Si ($\rho = 1\text{--}10 \text{ Ω cm}$), and the details of device fabrication and characterization can be found in the Supporting Information. Figure 1a shows a schematic of a typical monolayer graphene 1LG/Si device, and part b shows a digital photograph of device A. The energy band diagram, showing the Fermi levels of graphene ($E_f(\text{Gr})$) and lightly n-doped Si ($E_f(\text{Si})$) at thermal equilibrium (in a dark condition) is shown schematically in Figure 1c. From detailed measurements of the Schottky barrier heights (as discussed later on), we found that in our devices, $E_f(\text{Si})$ was pinned to the charge-neutrality level of its own surface states, with a Schottky barrier height $\phi_{bn} \sim 0.8$ V. Figure 1d shows the dark and low-power ($P = 1.23 \text{ μW}$, $\lambda = 488 \text{ nm}$) current–voltage (I – V) curves in device A, which follow a conventional rectifying and photodiode-like behavior, respectively. Incident photons generate e–h pairs in Si, and these photoexcited carriers thermalize rapidly to form quasi Fermi levels (separately for holes and electrons

near the valence and conduction band edges (VBE and CBE) of Si, respectively). The built-in electric field at the graphene/Si junction causes holes to inject out from Si (from the small energy-band between the VBE and quasi Fermi level for holes in Si) into graphene, which causes the appearance of a quasi Fermi level in graphene, $E'_f(\text{Gr})$. The position of the quasi Fermi level in graphene depends on (a) the position its bias-dependent $E_f(\text{Gr})$ and (b) the number of injected holes from Si. At low incident powers, $E'_f(\text{Gr})$ lies between $E_f(\text{Gr})$ and $E'_{fh}(\text{Si})$, and the photoexcited holes can all find accessible states in graphene to inject into, resulting in the conventional photodiode-like response. Figure 1e shows the I – V curves under increasing incident light powers (up to $P = 6.5 \text{ mW}$). At higher incident powers, there is a significant deviation of the I – V curves from the conventional photodiode-like response, with a strong suppression of photocurrents close to $V = 0$, and a sharp rise and rapid saturation of photocurrents at low reverse biases. This highly tunable photocurrent response is a result of the unique electronic structure of graphene near its Fermi level. Figure 1f schematically represents the situation under a low forward bias, V_{bias}^f , which lowers the Fermi level from its “unbiased” position. As seen in this figure, the lowering of the Fermi level brings it closer to the quasi Fermi level for holes in Si, greatly diminishing the number of accessible states for the photoexcited carriers to inject into from Si. Hence, under a forward bias, with increasing incident power and rate of hole-injection, $E'_f(\text{Gr})$ lowers and quickly aligns with the quasi Fermi level for holes in Si, $E'_{fh}(\text{Si})$ ($E'_f(\text{Gr}) = E'_{fh}(\text{Si})$, Figure

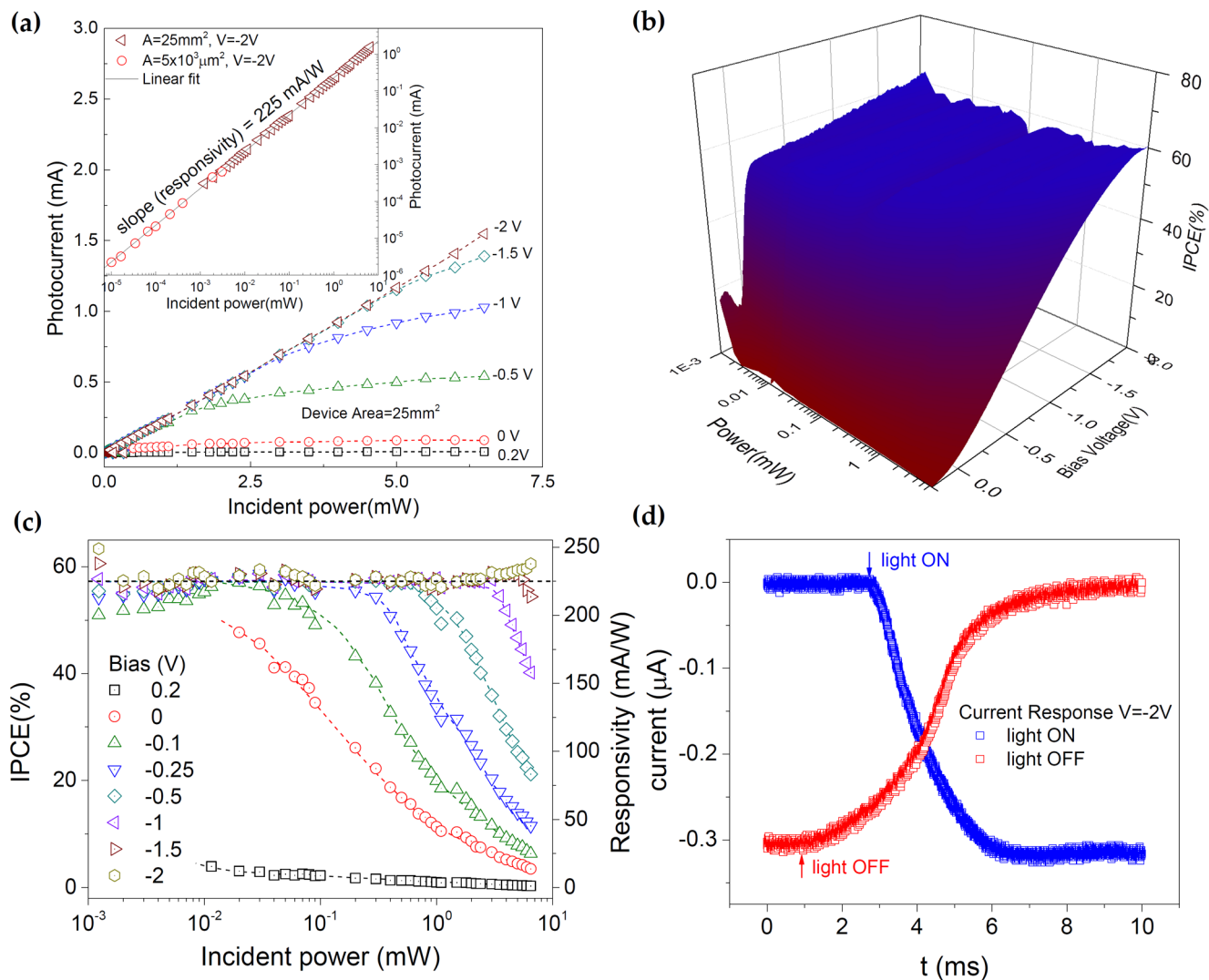


Figure 3. (a) The (dark-current subtracted) photocurrent (in device A) as a function of incident power for different applied voltages, showing strong voltage dependence at higher powers. The inset shows the photoresponse of both devices A and B. A device-independent responsivity of 225 mA/W was obtained at $V = -2$ V that remains constant over the entire range of powers we were able to test (~ 6 orders of magnitude). (b) IPCE map of device A, demonstrating the high photon-to-electron conversion efficiency of $\sim 57\%$ that can be tuned to remain constant over a large range of incident powers under reverse-bias operation. (c) Variation of IPCE as a function of the incident power at representative operational voltages in device A. The dashed lines are guides to the eye. The IPCE remains nearly unchanged at $V = -2$ V and goes $\rightarrow 0$ at $V = 0.2$ V. This small voltage range (-2 to 0.2 V) can be used as a switch to turn the photocurrent on and off with a high switching ratio ($>10^4$, see text). (d) Transient photocurrent response in device B, showing that the devices were capable of switching within a few milliseconds. In all cases, the incident light wavelength was 488 nm.

1f). Consequently, only a relatively small photocurrent (denoted by the small red part of the surface of the Dirac cone), limited by the small number of photoexcited holes that can inject into graphene, is possible under forward bias. Increasing the incident light power beyond this point will not allow any more photoexcited holes to inject into graphene since $E'_f(\text{Gr})$ cannot lie below $E'_{fh}(\text{Si})$. However, an applied reverse-bias can lift $E_f(\text{Gr})$ to higher values, as shown in Figure 1g, opening up a large number of accessible states for the holes to inject into and allowing a complete collection of the injected holes. As a result, the photocurrent, which is significantly suppressed near $V \approx 0$, can completely recover under small reverse biases, as seen in Figure 1e. (These deviations from a conventional photodiode behavior are explained with additional schematics in the Supporting Information document). The photocurrent saturates for a given incident power at higher

reverse biases (Figure 1e) when all photoexcited holes can inject into graphene. The photocurrent saturates for a given bias at higher incident powers (see later, Figure 3a) when the quasi-Fermi level in graphene, $E'_f(\text{Gr})$, reaches the quasi-Fermi level for holes in Si, $E'_{fh}(\text{Si})$. The voltage-induced tunability of the relative positions of the Fermi levels that enables a high photocurrent responsivity (see later), along with the low dark-current density ($\ll 1 \mu\text{A}/\text{cm}^2$), results in a tunable photocurrent ON/OFF ratio exceeding 10^4 at $V = -2$ V and at a light intensity of $260 \text{ pW}/\mu\text{m}^2$ making them highly suitable for low-power switches in micrometer-scale optoelectronic circuitry.

Figure 2a shows the photovoltage responsivity in device B as a function of incident power. At the lowest incident power, the absolute device responsivity $R_V (= V_{\text{OC}}/P, V_{\text{OC}}$ is the open circuit voltage) exceeds $10^7 \text{ V}/\text{W}$, which is significantly larger than that of previously reported graphene-based devices,⁷

rendering it a highly sensitive device for weak signal detection/switching/photometry. For applications such as weak-signal imaging, video-recording, or analytical chemistry, sensitivity to extremely small changes in incident power is another important parameter. To quantify this, we define the dynamic photovoltage responsivity or contrast sensitivity as dV_{OC}/dP . Figure 2b shows the contrast sensitivity in both devices A and B, measured over a broad range of incident powers. We find that the contrast sensitivity is remarkably independent of the device areas, exceeding 10^6 V/W at low light intensities. In addition, these devices show sharp rise in both the absolute and dynamic responsivity as the incident power decreases, which is a rather convenient feature appropriate for weak-signal detection.

For any photodetector, the detection limit is specified by the noise-equivalent-power (NEP),²³ which is the incident power at which the signal is equal to the RMS dark noise density (S_V), measured within a specified bandwidth (commonly 1 Hz), that is, $NEP = S_V/R_V$. To obtain S_V , a large sequence of voltage fluctuations (V_{noise}) was measured using a voltmeter set to 0.5 s integration time (which corresponds to a bandwidth of 1 Hz),²⁴ while keeping the device in darkness. The RMS noise density was then calculated as $S_V = (\langle V_{noise}^2 \rangle / 1 \text{ Hz})^{1/2}$. For the device B, we obtained $S_V = 1.66 \times 10^{-5}$ V/Hz^{1/2}. From the lowest measured power of 10 nW, $R_V \approx 1.8 \times 10^7$ V/W, and hence $NEP = 9.2 \times 10^{-13}$ W/Hz^{1/2} (implying that in the photovoltage mode, $P \sim$ piconWatt incidences can be detected above the noise level, when integrated over 0.5 s), and specific detectivity $D^* = (\text{device area})^{1/2}/NEP = 7.69 \times 10^9$ Jones (cm Hz^{1/2}/W). Further, at 10 nW incidence, $S_V/(dV_{OC}/dP) \approx 5$ pW/Hz^{1/2}, indicating that these detectors are capable of distinguishing materials with transmittance, $T = 0.9995$ (to compare, transmittance of monolayer graphene is about 0.977) within a 0.5 s integration time, making it extremely useful for absorption spectroscopy applications of ultradilute or ultrathin materials. We have also examined the transient-response time scale of these detectors, to ascertain how quickly they “switch” when an incident light is turned “on” or “off”. To do this, an optical chopper was placed in front of a laser source, and the photovoltage was recorded as a function of time using an oscilloscope triggered by the same chopper. Figure 2c and d show the photovoltage rise and fall response times obtained using a 50 ms timed optical chopper (which took about ~ 1.7 ms to completely chop the beam). In both cases, the response could be fitted to an exponential function as shown, with time scales of a few milliseconds (with the zero on the time axis corresponding to the point of opening and closing of the chopper). When tested at higher chopping speeds no change was found in the time-scale of the transient response, indicating that the response-time of a few milliseconds was intrinsic to the devices. We also note that the oscilloscope used had an input-impedance rated at $1\text{M}\Omega$ in parallel with a 20 pF capacitance. The effective time constant of the oscilloscope, $RC = 20 \times 10^{-6}$ seconds, is ~ 3 orders of magnitude smaller than the rise/fall time of the devices tested and hence did not affect detector transient response in any significant way. In addition, the long-term response to a periodically switching light was found to be extremely stable, with a variation of the OFF and ON state photovoltages well within $\pm 2.5\%$ and $\pm 5\%$, respectively, over 1000 switching cycles, and with absolutely no sign of drift or aging effects even after 10 days (see SI). The stable, millisecond level response is quite appealing for applications such as high-speed photography, videography, and rapid optical analysis of

chemical reactions that require tens of milliseconds of response time.

We now turn to the photocurrent response. Figure 3a shows the photocurrent I_{ph} as a function of incident powers for various biases in device A. In the inset, the response for $V = -2$ V has been plotted for both devices. We find that the response not only remains independent of device size but scales in an absolutely linear manner over six decades of incident power. The photocurrent responsivity of ~ 225 mA/W is 1–2 orders-of-magnitude higher than those of previously reported graphene-based photodetectors^{5–14} and a variety of normal-incidence (i.e., not waveguide coupled) Ge/Si photodetectors,²⁵ making it an extremely sensitive linear photodetector and photometer with a large dynamic range. The responsivity can be almost doubled at $\lambda = 850$ nm, as we show later. Also, the presented power range is only limited by our instrumental capabilities, and with higher reverse-biases, the linear response can potentially extend much beyond the experimentally tested range. The range-independent photocurrent responsivity and the $dV_{OC}/dP \sim 1/P$ dependence suggests that the underlying mechanism in our devices is photovoltaic^{5–8,10} and not hot-carrier-induced or photothermoelectric.^{9,11,14} Figure 3b is a 3D incident photon conversion efficiency ($IPCE(V,P) = (I_{ph}(V,P)/P) \times (hc/e\lambda)$) map of device A. By applying a low reverse bias, the device can operate with an $IPCE_{max} \sim 57\%$ over four orders-of-magnitude incident power. As shown in Figure 3c, by applying different biases, it is also possible to almost completely tune the IPCE between $0 < IPCE < IPCE_{max}$, which is extremely useful for brightness adjustment in imaging devices. Figure 3d shows the typical rise and fall times in response to a chopper. In this case, the responses could not be fitted to exponential functions. Nevertheless, it is clear that even in the case of photocurrent detection, the response is rapid enough (within a few milliseconds) for many imaging and analytical applications. The dark noise power spectral density (obtained in a manner similar to the one described earlier for S_V) was approximately $S_I = 11$ pA/Hz^{1/2}. For the undoped 1LG/Si device at 488 nm, this gave a $NEP = S_I/R_I = 50$ pW/Hz^{1/2}, which corresponds to a specific detectivity of 1.4×10^8 Jones (cm Hz^{1/2}/W), making it quite a sensitive photodetector even in the photocurrent mode. Moreover, the sensitive behavior of these detectors remain intact over the entire visible range of incident wavelengths, as seen from the spectral dependence of NEP and D^* in Figure 4, which is an important criterion for broadband imaging applications.

The photocurrent responsivity and hence conversion efficiencies could be further improved by increasing the graphene layer-thickness, and doping. Layer-thickening provides more states for the holes to inject into, and was achieved by multiple stacking of monolayer sheets of graphene. Doping the graphene sheets can be expected to increase their sheet conductance, and has been utilized in the past to enhance the performance of graphene/Si Solar cells.²¹ In our devices, p-type doping of the graphene sheets was obtained by drop-casting 1-pyrenecarboxylic acid (PCA), on the graphene sheets. In the past, we had reported how the π -stacking interaction between the pyrene part of PCA and graphene can lead to a stable but noncovalent attachment of these molecules to graphene and had performed extensive structural, electronic, optical, and electrochemical characterizations of PCA-functionalized graphene.^{26–28} In particular, we have found that attachment of PCA does not seem to have a very significant effect on the thickness of graphene layers²⁶ but increases the surface

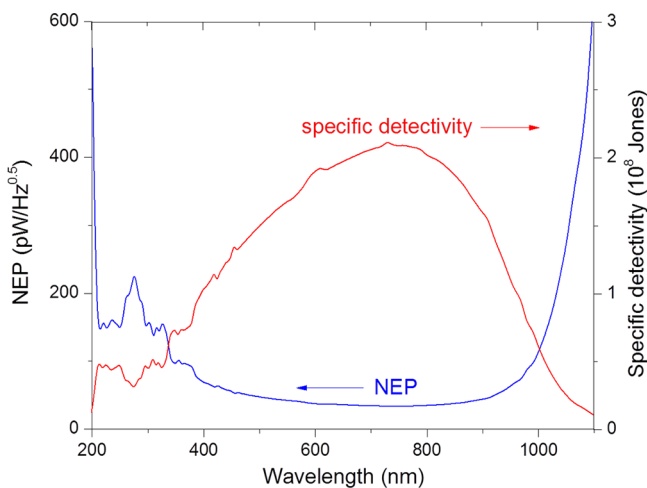


Figure 4. Spectral dependence of the noise-equivalent-power (NEP) and specific detectivity (D^*) of device B in the photocurrent mode. The minimum NEP and the maximum D^* were found to be 33 pW/Hz^{1/2} and 2.1×10^8 Jones, respectively, at $\lambda = 730$ nm.

roughness of graphene by about 0.2 nm (see SI). In addition, Raman spectra of PCA-doped graphene shows an increase in the D-band (see SI) that is most likely due to the presence of large number of edges in the graphene-like crystalline structure of pyrene. Figure 5a shows the resulting p-type doping effect of PCA on a separately prepared 3-terminal 1LG transistor. The drain current minimum of pristine graphene devices is at a positive voltage, indicating that the “pristine” graphene is already p-doped, either due to environment²⁹ or contaminant³⁰ effects. The application of PCA shifts the drain current minimum to higher gate voltage values, indicating an additional p-doping effect. Figure 5b and c compares the spectral dependence of IPCE and photocurrent responsivity in a three-layer graphene (3LG)/Si device (with and without doping) vis-à-vis the 1LG/Si device A, all of which had the same junction area. The IPCE of 3-layer graphene (3LG)/Si device improves over that of the 1LG/Si device, remaining at $\sim 60\%$ over a larger window of visible wavelengths. The corresponding responsivity grows to higher values (up to ~ 0.4 A/W at $\lambda = 885$ nm) in the 3LG/Si device, providing a greater

operational bandwidth compared to the 1LG/Si device. After PCA doping, the IPCE and responsivity values increase further over a large window of wavelengths, with maximum IPCE $\approx 65\%$ between 550 and 800 nm; and $R_i \approx 435$ mA/W for 850 nm $< \lambda < 900$ nm, making it highly appealing for on-chip applications that could benefit from the use of energy-efficient 850 nm VCSELs.³¹ We note that, as in the case of the 1LG/Si device, these improved responsivity/IPCE values could be seamlessly extended to high-power applications using low reverse biases (not shown).

Finally, we discuss the nature of the interface in these junctions. We have performed extensive measurements of the Schottky barrier height of these junctions, using graphene, doped graphene, and even control devices of Ti/Au with Si (to obtain the “metallic” side of the junction with a range of work-function values). Since p-doping lowers the Fermi level of graphene with respect to its Dirac point, one expects a larger Schottky barrier height,^{32–35} for the p-doped graphene samples. Surprisingly, we found that the Schottky barrier $\phi_{bn} = 0.79 \pm 0.05$ eV was nearly independent of the “metal” being used, a fact that can be traced to the nature of the graphene/Si junction.

In an ideal Si Schottky junction, the interfaces between the metal and Si is expected to be atomically clean to prevent the formation of any surface states on Si, resulting in the formation of an “unpinned” Schottky barrier junction,³⁶ whose barrier height $\phi_{bn} (= \phi_m - \chi_{Si})$ is dependent on the work-function of the metal, ϕ_m . In thermal equilibrium, the Fermi levels on both sides of the junction get aligned, and under illumination, behaves as conventional photodiodes with a reverse-bias independent photocurrent. In contrast, we believe that in our devices, the inadvertent formation of natural oxide on the Si surface, allows the energy bands in Si to naturally “pin” itself to its own surface states. This results in a Schottky barrier which is still rectifying but with a barrier-height which is pinned to its Bardeen limit of $\phi_{bn} \sim 0.8$ eV,³⁶ independent of the work function of the metal. With the Fermi level of Si pinned to its own charge-neutrality level, the thermal equilibrium position of the Fermi level of graphene at zero bias is determined by its own intrinsic doping level. UV-emission spectroscopy³⁷ has shown that CVD grown graphene can have work functions as high as 5.2 eV (due to substrate-induced effects), implying that

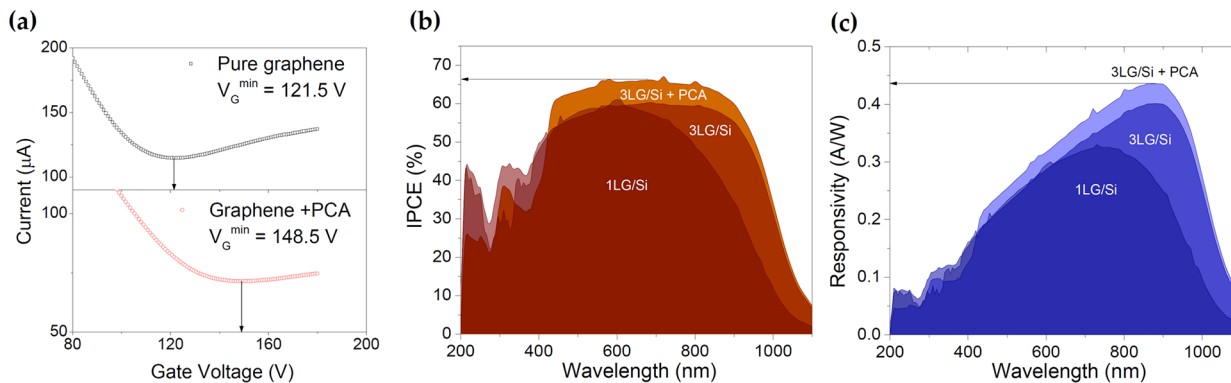


Figure 5. (a) Variation of drain–current as a function of gate voltage in a monolayer graphene 3-terminal transistor without and with PCA doping. The shift of the minima toward higher gate voltages is indicative of p-type doping due to PCA. (b) Spectral dependence of IPCE (200 nm $< \lambda < 1100$ nm) of device A (1LG/Si) versus a 3LG/Si device before and after doping with PCA. (c) Spectral responsivity for the same devices within the same wavelength window. The improved bandwidth and efficiency/response is clearly visible with increased layer thickness and doping. The doped 3LG/Si device has the best IPCE exceeding 60% over a broad range and with a maximum IPCE exceeding 65%. The responsivity peaks at ≈ 435 mA/W for 850 nm $< \lambda < 900$ nm.

the Fermi level can lie very close to the valence band edge of Si, effectively preventing the injection of photoinduced carriers into graphene under zero applied bias. We believe that this causes the suppressed photocurrent at zero-bias seen in our devices. This turns out to be an attractive feature, as it allows for an additional tunability of the photocurrent that results in the voltage-controllable responsivity discussed before.

Hence, graphene/Si heterojunctions can be used for a variety of tunable optoelectronic devices with high responsivities over a broad spectral bandwidth in the visible region. Their high responses and low dark-currents render them with a high switching ratio and low dark-power consumption. The picoWatt-level detection capability in both photovoltage and photocurrent modes along with linear operation demonstrated up to milliwatts of incident powers reflects a significantly large dynamic operational range. This, in addition to their millisecond-responses makes them versatile and highly sensitive photodetectors for a variety of imaging, metrology, and analytical applications over a broad range of input powers. The voltage-tunability allows brightness control for variable light conditions and enables linear operation over a large dynamic range. The responsivity peaking at 850 nm is ideal for coupling with VCSELs operating at these wavelengths³¹ for low-power integrated optoelectronic circuitry. Built using simple, low-cost, and scalable methods, additional improvements of CVD-graphene quality,³⁸ integration with waveguides,²⁵ and plasmonic^{7,8} or microcavity^{11,12} enhancements could lead to greater performances. Moreover, graphene junctions with other semiconductors such as Ge, GaAs, and so forth can provide further flexibility for controlling the peak-responsivity, spectral bandwidth, and high-speed operations.

■ ASSOCIATED CONTENT

■ Supporting Information

Experimental details about the synthesis of graphene and device fabrication; characterization of graphene samples; responsivity measurement as function of power and wavelength; time-dependent switching response; AFM and Raman characterization of PCA-doped graphene. This material is available free of charge via the Internet at <http://pubs.acs.org>.

■ AUTHOR INFORMATION

Corresponding Author

*E-mail: x.an@neu.edu (X.A.); s.kar@neu.edu (S.K.).

Notes

The authors declare no competing financial interest.

■ ACKNOWLEDGMENTS

We acknowledge the financial support provided by the Northeastern University start-up and internal seed grants provided to S.K. and Y.J.J. and partial support from an NSF award: ECCS-1202376.

■ REFERENCES

- (1) Yan, R.; Gargas, D.; Yang, P. Nanowire Photonics. *Nat. Photonics* **2009**, *3*, 569–576.
- (2) Konstantatos, G.; Howard, I.; Fischer, A.; Hoogland, S.; Clifford, J.; Klem, E.; Levina, L.; Sargent, E. H. Ultrasensitive solution-cast quantum dot photodetectors. *Nature* **2006**, *442*, 180–183.
- (3) Prins, F.; Buscema, M.; Seldenthuis, J. S.; Etaki, S.; Buchs, G.; Barkelid, M.; Zwiller, V.; Gao, Y.; Houtepen, A. J.; Siebbeles, L. D. A.; Zant, H. S. J. Fast and Efficient Photodetection in Nanoscale Quantum-Dot Junctions. *Nano Lett.* **2012**, *12*, 5740–5743.

- (4) Avouris, P.; Freitag, M.; Perebeinos, V. Carbon-nanotube Photonics and Optoelectronics. *Nat. Photonics* **2008**, *2*, 341–350.
- (5) Xia, F. N.; Mueller, T.; Lin, Y. M.; Garcia, A. V.; Avouris, P. Ultrafast graphene photodetector. *Nat. Nanotechnol.* **2009**, *4*, 839–843.
- (6) Muller, T.; Xia, F. N.; Avouris, P. Graphene Photodetectors for high-speed optical communications. *Nat. Photon.* **2010**, *4*, 297–301.
- (7) Echtermeyer, T. J.; Britnell, L.; Jasnos, P. K.; Lombardo, A.; Gorbachev, R. V.; Grigorenko, A. N.; Geim, A. K.; Ferrari, A. C.; Novoselov, K. S. Strong Plasmonic enhancement of photovoltage in graphene. *Nat. Commun.* **2011**, *2*, 458.
- (8) Liu, Y.; Cheng, C.; Liao, L.; Zhou, H.; Bai, J.; Liu, G.; Liu, L.; Huang, Y.; Duan, X. Plasmon resonance enhanced multicolour photodetection by graphene. *Nat. Commun.* **2011**, *2*, 579.
- (9) Gabor, N. M.; Song, J. C. W.; Ma, Q.; Nair, N. L.; Taychatanapat, T.; Watanabe, K.; Taniguchi, T.; Levitov, L. S.; Jarillo-Herrero, P. Hot carrier–assisted intrinsic photoresponse in graphene. *Science* **2011**, *334*, 648–652.
- (10) Park, J.; Ahn, Y. H.; Ruiz-vargas, C. Imaging of Photocurrent Generation and Collection in Single-Layer Graphene. *Nano Lett.* **2009**, *9*, 1742–1746.
- (11) Sun, D.; Aivazian, G.; Jones, A. M.; Ross, J. S.; Yao, W.; Cobden, D.; Xu, X. D. Ultrafast hot-carrier-dominated photocurrent in graphene. *Nat. Nanotechnol.* **2012**, *7*, 114–118.
- (12) Engel, M.; Steiner, M.; Lombardo, A.; Ferrari, A. C.; Löhneysen, H. v.; Avouris, P.; Krupke, R. Light–matter interaction in a microcavity-controlled graphene transistor. *Nat. Commun.* **2012**, *3*, 906.
- (13) Furchi, M.; Urich, A.; Pospischil, A.; Lilley, G.; Unterrainer, K.; Detz, H.; Klang, P.; Andrews, A. M.; Schrenk, W.; Strasser, G.; Mueller, T. Microcavity-Integrated Graphene Photodetector. *Nano Lett.* **2012**, *12*, 2773–2777.
- (14) Xu, X.; Gabor, N. M.; Alden, J. S.; Zande, A. M.; McEuen, P. L. Photo-Thermoelectric Effect at a Graphene Interface Junction. *Nano Lett.* **2010**, *10*, 562–566.
- (15) Konstantatos, G.; Badioli, M.; Gaudreau, L.; Osmond, J.; Bernechea, M.; Arquer, F. P. G.; Gatti, F.; Koppens, F. H. L. Hybrid graphene–quantum dot phototransistors with ultrahigh gain. *Nat. Nanotechnol.* **2012**, *7*, 363–368.
- (16) Nair, R. N.; Blake, P.; Grigorenko, A. N.; Novoselov, K. S.; Booth, T. J.; Stauber, T.; Peres, N. M. R.; Geim, A. K. Fine structure constant defines visual transparency of graphene. *Science* **2008**, *320*, 1308.
- (17) Novoselov, K. S.; Geim, A. K.; Morozov, S. V.; Jiang, D.; Zhang, Y.; Dubonus, S. V.; Grigorieva, I. V.; Firsov, A. A. Electric Field Effect in Atomically Thin Carbon Films. *Science* **2004**, *306*, 666–669.
- (18) Li, X.; Cai, W.; An, J.; Kim, S.; Nah, J.; Yang, D.; Piner, R.; Velamakanni, A.; Jung, I.; Tutuc, E.; Banerjee, S. K.; Colombo, L.; Ruoff, R. S. Large-Area Synthesis of High-Quality and Uniform Graphene Films on Copper Foils. *Science* **2009**, *324*, 1312–1314.
- (19) Chen, C.; Aykol, M.; Chang, C.; Levi, A. F. J.; Cronin, S. B. Graphene-Silicon Schottky Diodes. *Nano Lett.* **2011**, *11*, 1863–1867.
- (20) Li, X. M.; Zhu, H.; Wang, K.; Cao, A.; Wei, J.; Li, C.; Jia, Y.; Li, Z.; Li, X.; Wu, D. Graphene-on-silicon Schottky Junction Solar Cells. *Adv. Mater.* **2010**, *22*, 2743–2748.
- (21) Miao, X.; Tongay, S.; Petterson, M. K.; Berke, K.; Rinzler, A. G.; Appleton, B. R.; Hebard, A. F. High Efficiency Graphene Solar Cells by Chemical doping. *Nano Lett.* **2012**, *12*, 2745–2750.
- (22) Yang, H.; Heo, J.; Park, S.; Song, H. J.; Seo, D. H.; Byun, K. E.; Kim, P.; Yoo, I.; Chung, H. J.; Kim, K. Graphene Barristor, a Triode Device with a Gate-Controlled Schottky Barrier. *Science* **2012**, *336*, 1140–1143.
- (23) Richards, P. L. Bolometers for infrared and millimeter waves. *J. Appl. Phys.* **1994**, *76*, 1–24.
- (24) Shannon, C. E. Communication in the Presence of Noise. *Proc. IEEE* **1998**, *86*, 447–457.
- (25) Michel, J.; Liu, J.; Kimerling, L. C. High-performance Ge-on-Si photodetectors. *Nat. Photonics* **2010**, *4*, 527–534.

- (26) An, X.; Simmons, T.; Shah, R.; Wolfe, C.; Lewis, K. M.; Washington, M.; Nayak, S. K.; Talapatra, S.; Kar, S. Stable Aqueous Dispersions of Noncovalently Functionalized Graphene from Graphite and their Multifunctional High-performance Applications. *Nano Lett.* **2010**, *10*, 4295–4301.
- (27) An, X.; Bultler, T. W.; Washington, M.; Nayak, S. K.; Kar, S. Optical Sensing Properties of 1-Pyrenecarboxylic Acid Functionalized Graphene Films Laminated on Polydimethylsiloxane Membranes. *ACS Nano* **2011**, *5*, 1003–1011.
- (28) Ghosh, S.; An, X.; Shah, R.; Rawat, D.; Bakul, D.; Kar, S.; Talapatra, S. Effect of 1-Pyrene Carboxylic-Acid Functionalization of Graphene on Its Capacitive Energy Storage. *J. Phys. Chem. C* **2012**, *116*, 20688–20693.
- (29) Wehling, T. O.; Novoselov, S. V.; Vdovin, M. E. E.; Katsnelson, M. I.; Geim, A. K.; Lichtenstein, A. I. Molecular Doping of Graphene. *Nano Lett.* **2008**, *8*, 173–177.
- (30) Moser, J.; Barreiro, A.; Bachtold, A. Current-induced cleaning of graphene. *Appl. Phys. Lett.* **2007**, *91*, 163513.
- (31) Hofmann, W. H.; Moser, P.; Bimberg, D. Energy-Efficient VCSELs for Interconnects. *IEEE Photonics J.* **2012**, *4*, 652–656.
- (32) Liu, H.; Liu, Y.; Zhu, D. Chemical Doping of Graphene. *J. Mater. Chem.* **2011**, *21*, 3335–3345.
- (33) Shi, Y.; Kim, K. K.; Reina, A.; Hofmann, M.; Li, J. J.; Kong, J. Work Function Engineering of Graphene Electrode via Chemical Doping. *ACS Nano* **2010**, *4*, 2689–2694.
- (34) Tongay, S.; Schumann, T.; Miao, X.; Appleton, B. R.; Hebard, A. F. Tuning Schottky diodes at the many-layer-graphene/semiconductor interface by doping. *Carbon* **2011**, *49*, 2033–2038.
- (35) Cui, T.; Lv, R.; Huang, Z.; Zhu, H.; Zhang, J.; Li, Z.; Jia, Y.; Kang, F.; Wang, K.; Wu, D. Synthesis of nitrogen-doped carbon thin films and their applications in solar cells. *Carbon* **2011**, *49*, 5022–5028.
- (36) Sze, S. M. *Physics of Semiconductor devices*; Wiley-Interscience Publication: New York, 1981.
- (37) Park, J.; Lee, W. H.; Huh, S.; Sim, S. H.; Kim, S. B.; Cho, K.; Hong, B. H.; Kim, K. S. Work-Function Engineering of Graphene Electrodes by Self-Assembled Monolayers for High-Performance Organic Field-Effect Transistors. *J. Phys. Chem. Lett.* **2011**, *2*, 841–845.
- (38) Petrone, N.; Dean, C. R.; Meric, I.; Zande, A. M.; Huang, P. Y.; Wang, L.; Muller, D.; Shepard, K. L.; Hone, J. Chemical Vapor Deposition-Derived Graphene with Electrical Performance of Exfoliated Graphene. *Nano Lett.* **2012**, *12*, 2751–2756.